Journal of Alloys and Compounds 737 (2018) 530–535

Contents lists available at ScienceDirect

Journal of Alloys and Compounds

journal homepage: http://www.elsevier.com/locate/jalcom

Molybdenum incorporation on AB_2 alloys-Part II. On the synergetic effects of Laves and non-Laves phases

Erika Teliz [a], Joaquin Diez [a], Ricardo Faccio [b, c, d], Estefania German [b, c, d, e], Fernando Zinola [a], Verónica Díaz [f, *]

[a] Universidad de la República, Facultad de Ciencias, Laboratorio de Electroquímica Fundamental, Núcleo Interdisciplinario Ingeniería Electroquímica, Igua 4225, CP 11400, Montevideo, Uruguay
[b] Universidad de la República, Crystallography, Solid State and Materials Laboratory (Cryssmat-Lab), DETEMA, Facultad de Química, Montevideo, Uruguay
[c] Universidad de la República, Centro NanoMat, Polo Tecnológico de Pando, Facultad de Química, Montevideo, Uruguay
[d] Universidad de la República, Espacio Interdisciplinario, Facultad de Química, Montevideo, Uruguay
[e] Departamento de Física, Universidad Nacional del Sur & IFISUR (UNS-CONICET), Av. Alem 1253, 8000, Bahía Blanca, Argentina
[f] Universidad de la República, Facultad de Ingeniería, Instituto de Ingeniería Química, Núcleo Interdisciplinario Ingeniería Electroquímica, J. Herrera y Reissig 565, CP 11300, Montevideo, Uruguay

ARTICLE INFO

Article history:
Received 27 September 2017
Received in revised form
27 November 2017
Accepted 10 December 2017
Available online 12 December 2017

Keywords:
Molybdenum
Synergy
Laves phases
AB_2 alloys
Ni-MH batteries

ABSTRACT

Molybdenum substitution by chromium in $ZrCr_{1-x}NiMo_x$ alloys produces the segregation of Zr_xNi_y phases, $ZrCr_2$ and $ZrMo_2$ Laves phases as it was stated in Part I of this paper. In order to study the contribution of these phases in $ZrCr_{1-x}NiMo_x$ alloys performance, secondary Zr_9Ni_{11} and Zr_7Ni_{10}, together with $ZrCr_2$ and $ZrMo_2$ Laves phases were synthesized and their crystalline structures determined with XRD patterns. Zr_7Ni_{10} exhibits an orthorhombic structure, whereas Zr_9Ni_{11} depicts a tetragonal structure. $ZrCr_2$ presents a hexagonal structure (C14), while $ZrMo_2$ depicts a cubic structure (C15).

$ZrCr_2$ shows zero discharge capacities, while $ZrMo_2$ exhibits a first capacity value of 245 mAh g^{-1}. Zr_9Ni_{11} and Zr_7Ni_{10} phases exhibit maximum discharge capacities of 119 and 157 mAh g^{-1}, respectively.

Theoretical results show that the hydride stability for $ZrCr_2$ is larger than that for $ZrMo_2$. However, the great hydrogen storage capacity yields a slower desorption kinetics since it requires a considerable dehydrogenation energy. The opposite effect is observed for the proposed hexagonal structure $ZrMo_2$.

The 100% charge of the alloys shows different results for the hydrogen evolution reaction. Zr_7Ni_{10} phase depicts a better performance since the required potentials are lower than −1.05 V. There is a change in the rate determining step (*rds*) from a chemical recombination of surface hydrogen (Tafel pathway) in Zr_7Ni_{10} to a fast first electron transfer (Volmer step) for Zr_9Ni_{11}. Thus, the *rds* is strongly affected by the type of secondary phase dominant in each sample, being Zr_7Ni_{10} the most favorable.

1. Introduction

One of the most used technologies in hybrid electrical vehicles are nickel metal hydride batteries. AB_2 alloys are usually employed as negative electrodes in these batteries, which are composed by multi-element (like Zr and Ti for A atom and Cr, Ni, Mn and V for B atom), and multi-phase materials (integrated for Laves phases and secondary non-Laves phases) [1–5]. In this sense, it was demonstrated that the electrocatalytic performance of Zr-based alloys are based on the presence of Zr_8Ni_{21}, Zr_7Ni_{10}, Zr_9Ni_{11} and ZrNi as secondary phases [6–9]. For AB_2Zr/Ni based alloys, secondary non-Laves phases developed in addition to the main Laves phases, being Zr_7Ni_{10} and Zr_9Ni_{11}, those observed in a previous work [10]. It is worth noticing that kinetics and thermodynamics turns to be adverse after removing these secondary phases. Moreover, the deterioration of electrocatalytic properties is caused by the reduction of synergetic effects between the main storage and secondary non Laves phases [11–16]. The synergetic effects in metal hydride alloys refer to the existence of micro segregated secondary phases which provide beneficial effects. Synergetic effects were observed in the gaseous phase hydrogen storage as well as in the electrochemical environment improving the storage capacity and reversibility [17]. Besides, the learning on dissimilarities between

* Corresponding author.
E-mail address: verodiaz@fing.edu.uy (V. Díaz).

https://doi.org/10.1016/j.jallcom.2017.12.103
0925-8388/

synergetic effects in the two environments is a significant area of interest in recent works.

The term "synergetic effect" employed by Nei et al. [16] and clearly studied by Young et al. [18] is used to describe the discharge capacity enhancements or high-rate dischargeability (HRD) positively contributing to the overall performance of the AB_2 phase in the presence of Zr_xNi_y. The incidence of these phases offers additional catalytic sites for the gaseous phase hydrogen storage and electrochemical reactions [11–15]. Consequently, understanding these secondary phases conduct is crucial for future improvements of AB_2MH alloys. It can be observed that partial replacement of chromium by molybdenum (under the studied amounts) promotes the segregation of Zr_xNi_y phases [10].

Young et al. [18] presented a detailed work on the synergetic effects in an electrochemical environment. In the multi-phase system, the metal side with a higher work function along the grain boundary is supposed to be the first region that becomes hydrogenated and will not be totally dehydrided after 8 h in vacuum at 300 °C. The synergy in a multi-phase MH system can be explained by the pre-occupied hydrogen sites on the metallic side with a larger work function in close proximity to the grain boundary. Studies on this topic for MH alloys conclude that the catalytic phase must have a weaker M-H bond strength compared to that in the main storage phase. The C14 phase, with a stronger M-H bond, contributes to the reversibility in the hydrogen storage of other storage phases. The driving force for proton movement in the alloy varies for gaseous phase and electrochemistry. The former occurs by diffusion and the equilibrium with gaseous hydrogen at the clean surface, while the latter proceeds via the electric field and the local distribution of valence electrons.

In the present study, the investigation is focused on the micro segregated phases after molybdenum incorporation in $ZrCr_{1-x}NiMo_x$ alloys (named in part I as AB2M0 (Mo 0% w/w), AB2M1 (Mo 13% w/w) and AB2M2 (Mo 25% w/w)) and its effect on possible interactions and synergies. Besides, the effect of increasing amounts of molybdenum segregates different phases, thus, the effect of molybdenum with the advent of secondary phases, both of Laves ($ZrMo_2$ and $ZrCr_2$) and non-Laves ones (Zr_xNi_y) will be discriminated.

2. Experimental

2.1. Synthesis of alloys

Zr_7Ni_{10}, Zr_9Ni_{11} secondary phases as well as $ZrCr_2$ and $ZrMo_2$ Laves phases were synthesized. Synthesis method as well as electrode preparation for electrochemical characterization were just described in part I of this paper. Further details about hydride synthesis as well as the electrode preparation before pressing onto a nickel mesh were described elsewhere [19].

2.2. Structural and microstructural characterization of MH electrodes

The electrodes were characterized by X-ray diffraction using a Rigaku ULTIMA IV, 285 mm radius, powder diffractometer operating in Bragg Brentano geometry. CuK_α radiation ($\lambda = 1.5418$ Å), monochromatized with a diffracted beam bent germanium crystal, was used to collect data over the 10–110° 2θ range, in steps of 0.02°, using a scintillation detector. Fixed slits of 2/3° were used for data collection to prevent beam spillage outside the 2 cm long sample (along the beam-path) at low angles. The first step consisted of identifying the composition of samples and the determination of structures, which were similar in cell parameters and symmetry. After this, the structural models were prepared for the full pattern profile fitting, using the Rietveld method [20] by means of the EXPGUI-GSAS suite [21,22]. This methodology allowed extracting precise and relevant structural parameters and consistent weight crystalline fraction in the case of multiphase systems. Rietveld refinement was used to characterize the structure of the observed phases.

Before electrochemical testing of electrodes, the surface alloy microstructures were examined by means of a scanning electron microscope (SEM, JEOL JSM 5900) employing a 25 kV secondary electron imaging mode and energy dispersive spectroscopy (EDS) microanalysis.

2.3. Electrochemical characterization

Electrochemical measurements were run in a single compartment cell conventionally placing the working electrode (metal hydride electrode), counter electrode (nickel mesh) and reference electrode (Hg/HgO electrodes). In this work, potentials are referred to the Hg/HgO reference electrode and all the experiments carried out at room temperature. The electrolyte, 6M KOH solution, was prepared from reagent grade KOH and Millipore-MilliQ® plus water.

The electrodes were cycled for charge–discharge at constant current for 40 cycles. During charge–discharge experiments, constant density currents of −80 mA/g and 26 mA/g respectively were used, with a charge time of 5 h and a cut-off potential of −0.6 V, during discharge.

Self-discharge experiments were also performed. The rate at which a battery loses its power at open circuit is called the self-discharge rate. It is usually calculated from the lost discharge capacity after storage of fully charged MH electrodes to maximum discharge capacity after the activation by repeated charge–discharge cycling. Self-discharge rates after 84 h were calculated.

Linear sweep voltammetry was conducted on each surface (for SOC 100%) starting from open circuit potential and scanning towards cathodic values up to −1.3 V run at 0.001 V s^{-1}. The electrochemical characterization of the alloys was completed by cyclic voltammetry in the supporting electrolyte run between −0.6 V and 1.3 V at 0.001 V s^{-1}. All the electrochemical experiments were conducted using a PGZ 301 Voltalab® potentiostat-galvanostat device.

2.4. Computational section

In part I it was demonstrated that the electrocatalytic performance of $ZrCr_{1-x}NiMo_x$ alloys are strongly dependent on structural microsegregated phases. X-ray diffraction (XRD) characterization at the National Synchrotron Light Laboratory (LNLS) in Campinas revealed the existence of $ZrCr_2$ and $ZrMo_2$ as Laves phases in molybdenum containing alloys. Density Functional Theory (DFT) calculations [23,24] were performed for the study of structural and electronic properties of hydrogenated $ZrCr_2$ and $ZrMo_2$ phases employing the projector-augmented wave (PAW) method [25,26] as implemented in the Vienna *ab-initio* simulation package VASP [27]. An energy cutoff of 500 eV was used to expand the Kohn-Sham orbitals into plane wave basis sets. In addition, the semicore states of Cr, Mo and Zr have been explicitly treated as valence states throughout this work. In all of the calculations reported here, GGA-PBE exchange-correlation functional [28,29] is selected. A Monkhorst-Pack k-point mesh [30] equivalent to $4 \times 4 \times 4$ was taken for the full (reducible) Brillouin Zone, allowing the convergence of total energy and forces. The start point was the reported crystal structures of $ZrCr_2$ and $ZrMo_2$ in its hexagonal crystal system. Then, dimension and ion positions were allowed to be optimized, until residual forces and stress tensor components were positioned down to 0.01 eV/Å and 5 kbar respectively.

Consecutively hydrogen was added to these structures determining the conforming formation energy from the reaction: $ZrM_2+n/2H_2 \rightarrow ZrM_2H_n$ (M = Cr; Mo), using the following formula; $E_{form} = -(E(ZrM_2H_n) - (n/2*E(H_2)) - E(ZrM_2))$.

3. Experimental results

3.1. Metallurgical characterization

Microstructures of Zr_7Ni_{10}, Zr_9Ni_{11} secondary phases, as well as $ZrCr_2$ and $ZrMo_2$ alloys, are analyzed by SEM (back-scattered electrons, BSE). From EDS results analysis, it was concluded that the stoichiometry for the studied alloys was the expected one. XRD studies shows that Zr_7Ni_{10} presents an orthorhombic crystalline system structure with a *Pbca* spatial group. On the other hand, Zr_9Ni_{11} depicts a tetragonal crystalline system structure with *I4/m* as spatial group. These structures correspond with those found as secondary phases in AB2M0, AB2M1 and AB2M2 samples.

Besides, $ZrCr_2$ and $ZrMo_2$ samples match, as expected, to Laves phases. $ZrCr_2$ presents a hexagonal crystalline system structure (C14), spatial group: $P6_3/mmc$, while $ZrMo_2$ depicts a cubic crystalline system structure (C15) with $Fd\bar{3}m$ as spatial group.

AB_2 hysteresis would not be related with multiphase's existence or molybdenum content because AB2M0 and AB2M2 hysteresis values are similar and larger than the AB2M1 value [31]. Young et al. [32–34] stated that in ternary alloys and in $Ti_{12.5}Zr_{21}V_{10}Cr_{8.5}Mn_x$-$Co_{1.5}Ni_{46.5-x}$ AB2 type, with C14 Laves main phase, hysteresis in P-c-T curves decrease when a/c ratio increase. From previous results [10] a/c ratio was calculated resulting in 0.6105, 0.6115 and 0.6094 for AB2M0, AB2M1 and AB2M2 respectively.

It is worthwhile noticing that $ZrCr_2$ *a/c* ration is higher than those previously reported for C14 Laves presented in AB2M0, AB2M1 and AB2M2, 0.617. This fact could explain why AB2M1 depicts the smallest hysteresis [31]. Moreover, it could also give details about the fact that AB2M2 hysteresis is similar to that of AB2M0, though the former alloy presents a larger heterogeneity and minor amounts of Lave phases in its composition.

3.2. Electrochemical characterization

Discharge capacities of the alloys samples are reported as a function of the number of charge-discharge cycles in Table 1.

As far as secondary phases are concerned, Zr_7Ni_{10} has the largest capacity. However, its activation takes approximately 50 cycles. On the other hand, $ZrMo_2$ phase activates at the first cycle and later decrease as a result of KOH reactivity (this phase is unstable in KOH 6M, it presents corrosion). Besides, $ZrCr_2$ depicts almost zero discharge capacity. This phase has very low equilibrium pressure and thus, a very high equilibrium potential. Therefore, it could not reach hydrogenation and will not be totally de-hydrided after experimental conditions.

From these results it can bring to a close that the smaller discharge capacity value of AB2M2 alloy could be related to its high content of $ZrCr_2$ phase. On the other hand, although $ZrMo_2$ sample depicts an unstable behavior, it could be shielded, forming the matrix alloy without being in contact with the corrosive environment. In this way its presence could improve the discharge capacity.

Table 1
Discharge capacity (C_{dis}/mAh g^{-1}) for $ZrCr_2$, $ZrMo_2$, Zr_9Ni_{11} and Zr_7Ni_{10} alloys at distinct charge/discharge cycles: 1, 3, 10, 30 and 50.

	$C_{dis}(1)$	C_{dis} (3)	$C_{dis}(10)$	$C_{dis}(30)$	$C_{dis}(50)$
$ZrCr_2$	3	7	8	7	7
$ZrMo_2$	245	50	6	X	X
Zr_9Ni_{11}	4	7	32	80	119
Zr_7Ni_{10}	3	6	36	111	157

Non-Laves secondary phases Zr_9Ni_{11} and Zr_7Ni_{10}, depict a maximum discharge capacity of 119 mAh/g and 157 mAh/g, respectively. Fig. 1a shows the discharge capacity *vs.* the number of cycles. From these preliminary results we can bring to at least two conclusions: (a) Zr_7Ni_{10} phase depicts the highest storage capacity, explaining the highest discharge value presented in AB2M1 alloy and (b) AB_2 activation process is not related to secondary phases but it is a strong evidence of the influence of Laves phases containing molybdenum ($ZrCr_{1-x}Mo_xNi$ and $ZrMo_2$).

Charge ending potential and half-discharge potential evolution with the number of charge-discharge cycles is presented in Fig. 1b. Both alloys depict the same profile. Consequently, the fact that AB2M1 has a charging potential closer to the reversible value than that of the AB2M0 sample could not be possibly related to Zr_XNi_y secondary phases. Overpotential decrease was more significant in AB2M1 alloy and this sample also depicted the lowest overpotential value, both aspects should be associated with the presence of Laves phases containing molybdenum ($ZrCr_{1-x}Mo_xNi$ and $ZrMo_2$).

It is worth noticing that although AB2M2 alloy presents $ZrCr_{1-x}Mo_xNi$ and $ZrMo_2$ Laves phases, it depicts the smallest discharge capacity as well as the biggest ΔE (Fig. 1b). This behavior could be related to weight composition of Laves phases (including $ZrCr_2$) in the alloy, which is only 35%, meanwhile secondary phases represent almost 65%. Accordingly, molybdenum incorporation induces secondary phase segregations as well as molybdenum containing Laves phases and $ZrCr_2$ formation. It can be concluded that there is a compromise between molybdenum concentration and the percentage of Laves phases that is lost by the segregation of secondary phases.

Cyclic voltammetries were carried out for Zr_9Ni_{11} and Zr_7Ni_{10} samples in alkaline solutions at 0.001 Vs^{-1} (Fig. 2). Hydrogen evolution current intensity for Zr_9Ni_{11} is significantly higher than for Zr_7Ni_{10} from −1.09 V potential values. Between −0.87 V and −1.09 V, the observed behavior is opposite. On the other hand, Zr_9Ni_{11} anodic charge is smaller in accordance to a minor hydrogen discharge capacity.

In order to study the effect of Zr_xNi_y phases on hydrogen evolution mechanism a linear sweep voltammetry was carried out. For a SOC of 100%, a linear polarization at 0.001 Vs^{-1} from open circuit potential (E_{OPC}) to −1.3 V was conducted in both alloys. The semi-logarithm plots, Tafel lines, are depicted in Fig. 3 for the Zr_7Ni_{10} and Zr_9Ni_{11} alloys.

Linear sweep voltammetric profiles of these alloys could explain the observed AB2M0, AB2M1 and AB2M2 specimen behavior during charge processes (Part I). Zr_7Ni_{10} secondary phase depicts the best performance during hydrogen evolution for potential values smaller than −1.05 V.

Tafel slopes were determined and evaluated from polarization curves and further depicted in Fig. 3 (right Panel), being ca. −0.120 V dec^{-1} in both alloys. It is worth noticing that Zr_7Ni_{10} depicts a second slope of −0.060 $Vdec^{-1}$ at lower overpotentials. These results evidence a change in *rds* mechanism for Zr_7Ni_{10} due to phase transitions inside the hydride alloy, manifested then at the surface of the electrode. The value *RT/F* denotes a chemical *rds* after a fast first electron transfer step or an electrochemical single electron transfer step with the adsorbed intermediate coverage value obeying the Temkin or Frumkin type isotherm (Tafel step) instead of simple langmuirian conditions. The −0.120 V dec^{-1} value responds to a *rds* typical of the electrochemical charge transfer pathway (Volmer Reaction), *i.e.* the first electron transfer as *rds*. From AB2M0, AB2M1 and AB2M2 alloys Tafel line results (Fig. 5 Part I); it can be concluded that mechanism reaction strongly depends on secondary phases in the alloy, being Zr_7Ni_{10} the one with the best behavior.

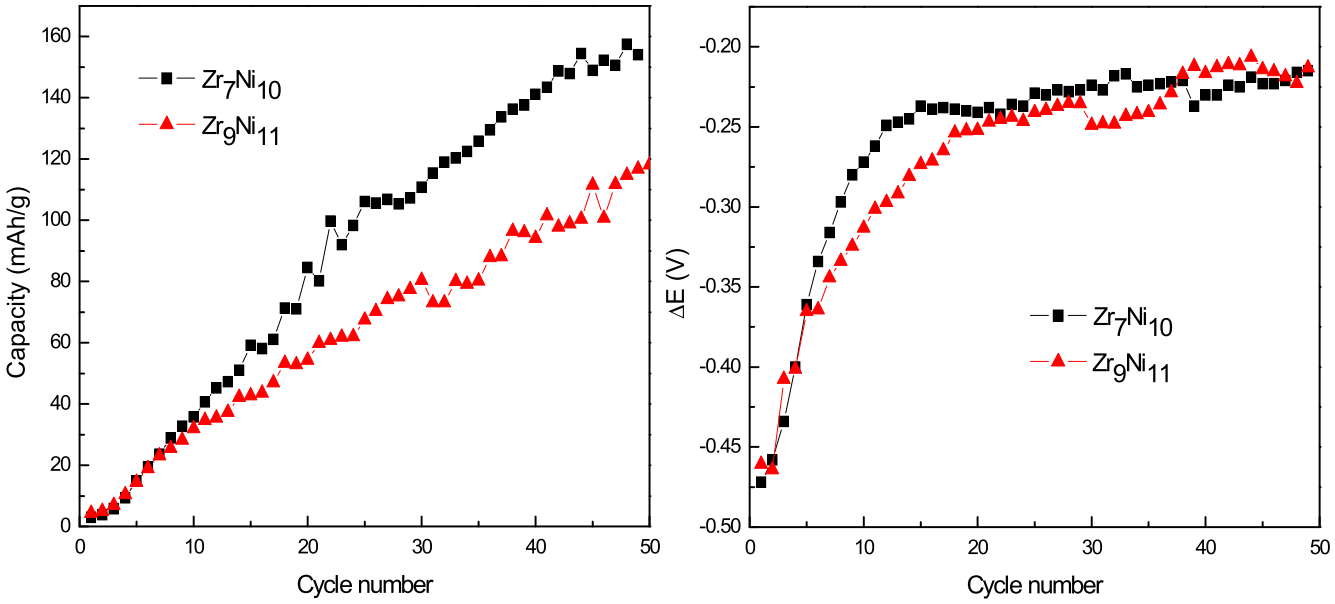

Fig. 1. a. Activation curve: discharge capacity (mA h g^{-1}) *vs.* Number of cycles (left Panel). b. End and middle charge potential difference, ΔE *vs.* Number of cycles (right Panel) for Zr_7Ni_{10} and Zr_9Ni_{11} alloys.

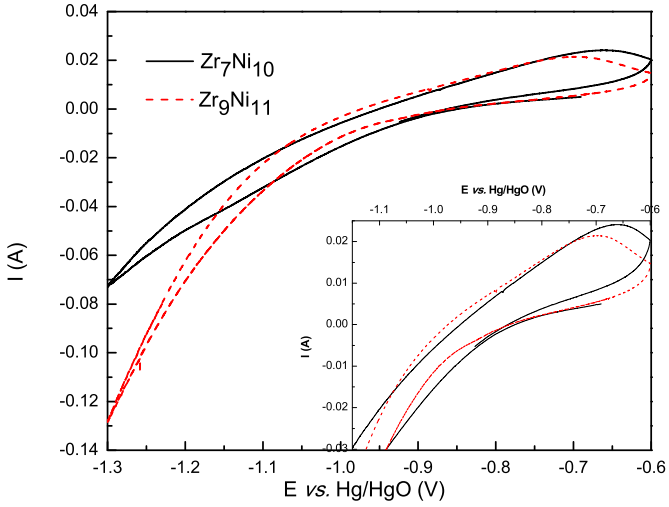

Fig. 2. Cyclic voltammetry between −0.6 and 1.3 V run at 1 mV/s for Zr_7Ni_{10} and Zr_9Ni_{11} alloys.

Self-discharge plots for Zr_9Ni_{11} and Zr_7Ni_{10} secondary phases are presented in Fig. 4. The capacity decay profiles for both secondary phases are similar, after 80 hs the observed retention capacity is nearly 70%. AB2M0 depicted the same behavior meanwhile for AB2M1 and AB2M2 capacity retentions are nearly 80% after the same time. From these results we can bring at least to this conclusion: AB_2 self-discharge behavior depends on the presence of $ZrCr_{1-x}Mo_xNi$ and $ZrMo_2$ specimens.

4. Computational results

The studied $ZrMo_2$ and $ZrCr_2$ structures were modeled using a cell containing 12 atoms, namely, 4 Zr atoms and 8 Mo or Cr atoms in its hexagonal crystal system (Fig. 5). The hydrogen occupation in these structures was studied adding from 1 to 30 H atoms, *i. e.* from an occupation of 0.25–7.50. These hydrogen atoms can occupy not only hexagonal but also trigonal positions (see Fig. 5).

After each H addition, the system was allowed to relax and the corresponding occupation energy was calculated with the following equation:

$$E = -(E_{AB2+nH} - (n/2{*}E_{H2}) - E_{AB2}) \quad (1)$$

being E_{AB2+nH} the energy of AB_2 structure plus n H atoms, E_{H2} the energy of a molecule of hydrogen gas and E_{AB2} the energy of the system without hydrogen atoms.

As it was said above, theoretical calculations were carried out to study the hydrogenation thermodynamics in these $ZrCr_2$ and $ZrMo_2$ structures in a hexagonal crystal system. Despite $ZrMo_2$ is cubic in its electronic ground state, the aim of this work is to study the effects of molybdenum addition in hexagonal phases and to strictly evaluate the effect of the 3*d* metal.

First, the geometric optimization of pure $ZrCr_2$ and $ZrMo_2$ structures were performed. Then, hydrogen atoms were gradually added to the systems and formation enthalpies were calculated according to:

$$ZrM_2 + nH_2 \rightarrow ZrM_2H_{2n} \quad (M = Cr \text{ and } Mo) \quad (2)$$

n takes values from 1/2 to 15, giving a number of hydrogen atoms in the systems from 1 to 30 (*i.e.* occupations from 0.25 to 7.50). In every case, apart positions were selected to avoid H-H interaction, while H was added (see numbering Fig. 5).

When the first H atom is added, it can be seen that every site is energetically equivalent, showing a slight preference to hexagonal sites. Thus, it was found energies of 0.544 eV and 0.500 eV for $ZrCr_2$; 0.533 eV and 0.460 eV for $ZrMo_2$, for hexagonal and trigonal sites, respectively.

Two ways to analyze H addition were studied. The first one was taking as initial point the previous relaxed structure, that is to say, H addition in AB_2+nH relaxed structure and the second way was to add H atoms in the not-relaxed AB_2+nH structure. In the first case, the added H atoms diffuse easily in the structure from one site to another, changing significantly the final structures. The second case allows us to understand the behavior of AB_2 structures when H is added. As it can be seen in Fig. 6, the curve energy *vs.* H occupation, and Table 2, the maximum peaks are in 5.00 H occupation for $ZrCr_2$

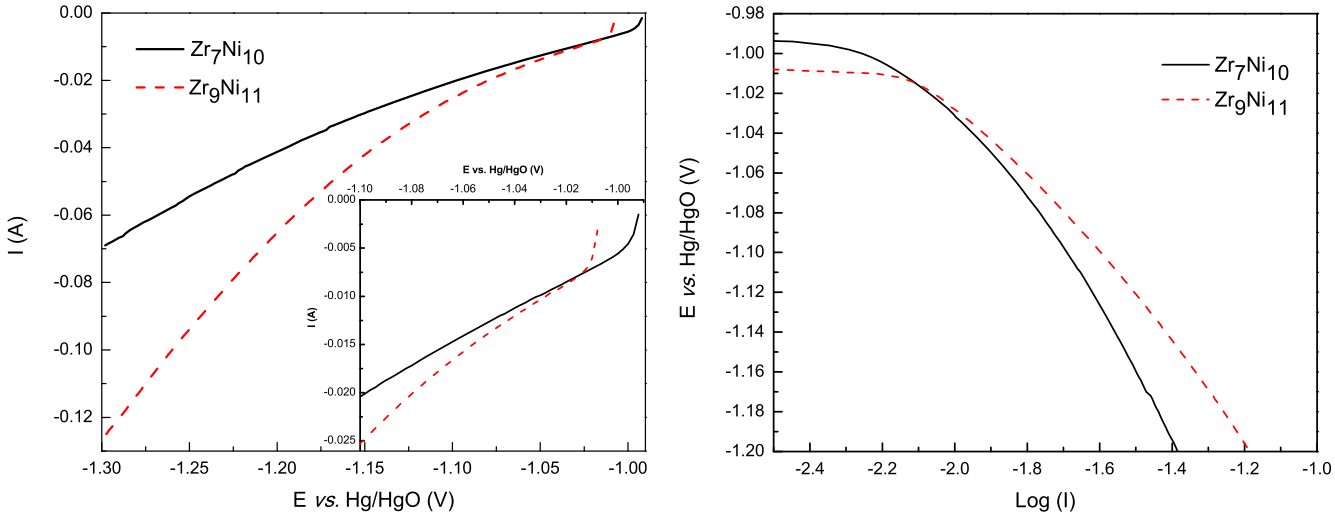

Fig. 3. Linear sweep voltammetry (left Panel) and Tafel plot (right Panel) for Zr_7Ni_{10} and Zr_9Ni_{11} alloys.

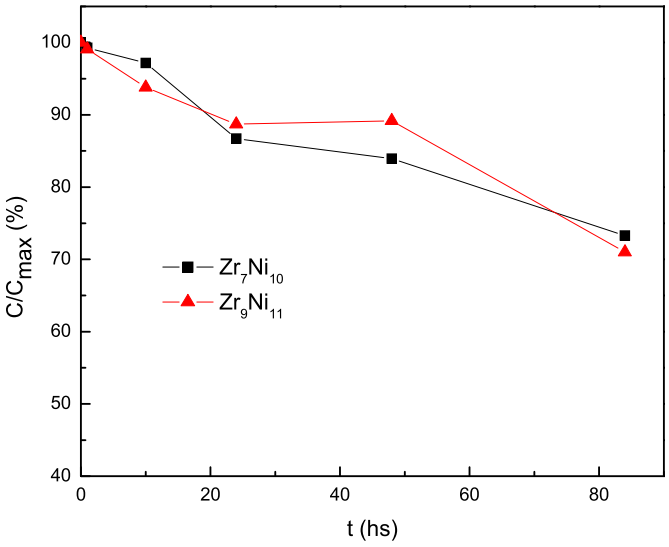

Fig. 4. Percentage of retention capacity *vs*. Rest time for Zr_7Ni_{10} and Zr_9Ni_{11} alloys.

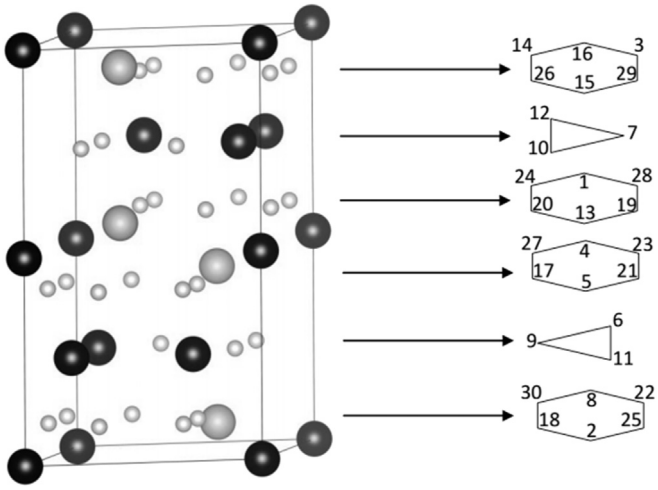

Fig. 5. AB_2 hexagonal system and possible hydrogen positions. Grey spheres represent Zr atoms, black spheres stand for Mo or Cr and white spheres correspond to H atoms. Numbering of the order of H filling is included.

and 2.50 for $ZrMo_2$, this corresponds to 20 and 10 H atoms in the AB_2 structures, respectively.

Results show that the hydride stability for $ZrCr_2$ is significantly bigger than hydride stability for $ZrMo_2$. The first one has a larger hydrogen storage capacity, therefore the energy needed for de-hydrogenation is high, making the desorption kinetics slower. Hexagonal $ZrMo_2$ presents the opposite effect. The presence of $ZrCr_2$ phases in the samples diminishes its storage capacity and increases its overpotential, as it is observed in AB2M2 alloy.

Moreover, calculations indicate that an optimum load for every phase exists; this is higher for $ZrCr_2$ in comparison with the case of $ZrMo_2$. In both samples, hydrogen occupation energy becomes unfavorable around 5.00. This demonstrates that hydrogen storage thermodynamics is better for $ZrCr_2$ than $ZrMo_2$, however strong thermodynamic stability affects negatively the discharge capacity of this alloy.

5. Part II summary

- Secondary and Laves phases were synthesized, that is, $ZrCr_2$, $ZrMo_2$, Zr_9Ni_{11} and Zr_7Ni_{10}. The latter exhibits an orthorhombic structure with a *Pbca* spatial group, whereas Zr_9Ni_{11} depicts a tetragonal structure withaI4/m spatial group. $ZrCr_2$ presents a hexagonal structure (C14), while $ZrMo_2$ depicts a cubic structure (C15).
- $ZrCr_2$ shows zero discharge capacities while $ZrMo_2$ exhibits a value of 245 $mAhg^{-1}$during the first cycle, which decays to 50 $mAhg^{-1}$during the second cycle (20% of the initial figure). Zr_9Ni_{11} and Zr_7Ni_{10} secondary phases present a maximum discharge capacity of 119 and 157 $mAhg^{-1}$, respectively, with the same number of cycles to activate under similar ΔE values.
- Upon charging processes in the alloys, the Zr_7Ni_{10} phase depicts a better performance for hydrogen evolution reaction since the involved potentials are lower than −1.05 V. From Tafel plots for Zr_7Ni_{10} and Zr_9Ni_{11} it was observed a change in the *rds* from a chemical recombination of surface hydrogen (Tafel pathway) in Zr_7Ni_{10} to a fast first electron transfer (Volmer step) for Zr_9Ni_{11}. Thus, the *rds* is strongly affected by the type of secondary phase dominant in each sample, being Zr_7Ni_{10} the most favorable.
- Secondary phases exhibit similar self-discharge capacity curves and comparable to that obtained in the absence of molybdenum. For 84 hs of rest time, the three samples with different amounts of molybdenum showed a retention capacity of 71% in the

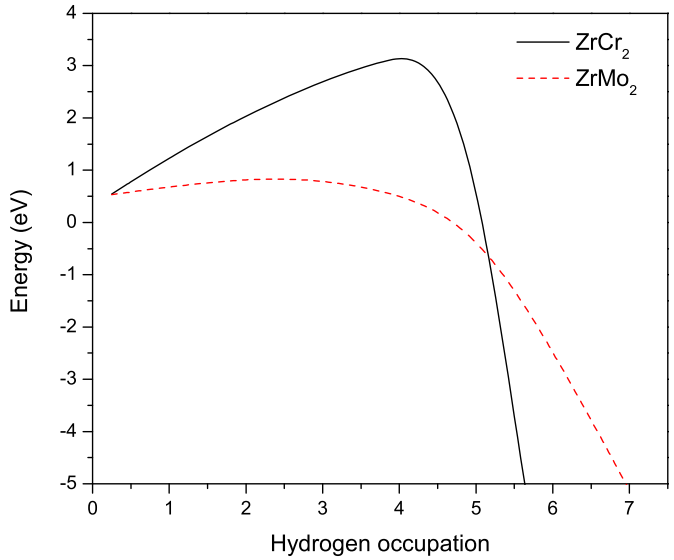

Fig. 6. Formation energy *vs*. Hydrogen occupation curves for $ZrCr_2$ and $ZrMo_2$ systems.

Table 2
Formation energy calculated for different H occupation for studied systems.

H occupation	E_{form} (eV)	
	$ZrCr_2$	$ZrMo_2$
0.25	0.544	0.533
1.25	1.479	0.735
2.50	2.415	0.890
3.75	3.132	0.670
5.00	3.421	0.017
6.25	−13.475	−3.064
7.50	−7.029	−6.486

absence of molybdenum and 82% for the others. This shows that the self-discharge behavior for all AB_2 alloys is directly related to the presence of $ZrCr_{1-x}Mo_xNi$ and $ZrMo_2$.

➢ Theoretical results show that the hydride stability for $ZrCr_2$ is significantly bigger than that for $ZrMo_2$. However, this larger hydrogen storage capacity yields a slower desorption kinetics since the de-hydrogenation energy needed is too high. The opposite effect is observed for the proposed hexagonal structure $ZrMo_2$. It can be concluded that the presence of $ZrCr_2$ phases in the samples diminishes its hydrogen storage capacity and increases the hydrogen overpotential.

6. Global conclusions

From discharge capacity results it can be concluded at least three facts:

(a) Zr_7Ni_{10} phase depicts the highest hydrogen storage capacity which could explain why AB2M1 discharge capacity is larger than AB2M0 and AB2M2.
(b) Although AB_2 activation process is not related to secondary phases, evidence of the positive influence of molybdenum containing Laves phases ($ZrCr_{1-x}Mo_xNi$ and $ZrMo_2$) was found.
(c) Small ΔE values reported in AB2M1 sample could be associated with Laves phases $ZrCr_{1-x}Mo_xNi$ and $ZrMo_2$.

There is an optimum amount of molybdenum after its substitution by chromium since it produces the segregation of phases of the Zr_xNi_y type as well as Laves phases $ZrCr_2$ and $ZrMo_2$. The presence of $ZrCr_2$ is clearly not good since it produces a decrease in the proportion of Laves phases with a lesser hydrogen storage capacity.

On the other hand, $ZrCr_{0.7}Mo_{0.3}Ni$ with 13% weight in molybdenum is the one that exhibits the best results, since it exhibits a compromise between Zr_7Ni_{10} phase and Laves phases with molybdenum ($ZrCr_{1-x}Mo_xNi$ and $ZrMo_2$) with little presence of $ZrCr_2$. Thus, the alloy with 13% weight in molybdenum is the one presenting the best thermodynamic and kinetic behavior for hydrogen storage purposes.

Acknowledgements

The authors wish to thank ANII, UDELAR and PEDECIBA for the financial support and academic representations and Dr. F.C. Ruiz to enable the alloys in bicollaboration. Dr. E. German and R. Faccio would like to thank (ANII) Post-doc “Fondo Professor Dr. Roberto Caldeyro Barcia” code PD_NAC_2015_1_108133.

References

[1] M.A. Fetcenko, S.R. Ovshinsky, K. Young, B. Reichman, C. Fierro, J. Koch, F. Martin, W. Mays, T. Ouchi, B. Sommers, A. Zallen, J. Alloys Compd. 330/332 (2002) 752–759.
[2] M.A. Fetcenko, S.R. Ovshinsky, B. Reichman, K. Young, C. Fierro, J. Koch, A. Zallen, W. Mays, T. Ouchi, J. Power Sources 165 (2007) 544–551.
[3] K. Young, B. Chao, Y. Liu, J. Nei, J. Alloys Compd. 606 (2014) 97–104.
[4] K. Young, T. Ouchi, B. Huang, B. Reichman, M.A. Fetcenko, Int. J. Hydrogen Energy 36 (2011) 12296–12304.
[5] K. Young, T. Ouchi, A. Banik, J. Koch, M.A. Fetcenko, Int. J. Hydrogen Energy 36 (2011) 3547–3555.
[6] K. Young, J. Nei, T. Ouchi, M.A. Fetcenko, J. Alloys Compd. 509 (2011) 2277–2284.
[7] K. Young, T. Ouchi, B. Huang, B. Reichman, M.A. Fetcenko, J Power Sources 20 (2011) 8815–8821.
[8] F.C. Ruiz, E.B. Castro, H.A. Peretti, A. Visintin, Int. J. Hydrogen Energy 35 (2010) 9879–9887.
[9] K. Young, M. Young, S. Chang, B. Huang, J. Alloys Compd. 560 (2013) 33–41.
[10] E. Teliz, R. Faccio, F. Ruiz, C.F. Zinola, V. Diaz, J. Alloys Compd. 649 (2015) 267–274.
[11] W.K. Zhang, C.A. Ma, X.G. Yang, Y.Q. Lei, Q.D. Wang, G.L. Lu, J. Alloys Compd. 293–295 (1999) 691–697.
[12] Q.A. Zhang, Y.Q. Lei, X.G. Yang, K. Ren, Q.D. Wang, J. Alloys Compd. 292 (1999) 241–246.
[13] F.C. Ruiz, E.B. Castro, S.G. Real, H.A. Peretti, A. Visintin, W.E. Triaca, Int. J. Hydrogen Energy 33 (2008) 3576–3580.
[14] K. Young, T. Ouchi, B. Huang, B. Chao, M.A. Fetcenko, L.A. Bendersky, K. Wang, C. Chiu, J. Alloys Compd. 506 (2010) 841–848.
[15] K. Young, J. Nei, B. Huang, M.A. Fetcenko, Int. J. Hydrogen Energy 36 (2011) 11146–11154.
[16] J. Nei, K. Young, R. Regmi, G. Lawes, S.O. Salley, K.Y.S. Ng, Int. J. Hydrogen Energy 37 (2012) 16042–16055.
[17] K. Young, T. Ouchi, T. Meng, D.F. Wong, Batteries 15 (2016) 2–22.
[18] K. Young, M. Young, S. Chang, B. Huang, J. Alloys Compd. 560 (2013) 33–41.
[19] K. Petrov, A. Rostami, A. Visintin, S. Srinivasan, J. Electrochem. Soc. 141 (1994) 1747.
[20] H.M. Rietveld, J. Appl. Cryst. 2 (1969) 65.
[21] A.C. Larson, R.B. Von Dreele, General Structure Analysis System (GSAS), Los Alamos National Laboratory Report LAUR, 2000, pp. 86–748.
[22] B.H. Toby, J. Appl. Crystallogr. 34 (2001) 210.
[23] P. Hohenberg, W. Kohn, Inhomogeneous electron gas, Phys. Rev. 136 (3B) (1964) B864–B871.
[24] W. Kohn, L. Sham, J. Phys. Rev. 140 (4A) (1965) A1133–A1138.
[25] P.E. Blöchl, Phys. Rev. B 50 (24) (1994) 17953–17979.
[26] G. Kresse, J. Furthmüller, Comput. Mater. Sci. 6 (1) (1996) 15–50.
[27] G. Kresse, D. Joubert, Phys. Rev. B 59 (3) (1999) 1758–1775.
[28] J.P. Perdew, K. Burke, M. Ernzerhof, Phys. Rev. Lett. 77 (1996) 3865.
[29] J.P. Perdew, K. Burke, M. Ernzerhof, Phys. Rev. Lett. 78 (1997) 1396. H.J.
[30] Monkhorst, J.D. Pack, Phys. Rev. B 13 (1976) 5188–5192.
[31] C.F. Zinola, V. Diaz, E. Teliz, J. Electrochem. Soc. 163 (2016) A2579–A2585.
[32] K. Young, T. Ouchi, M.A. Fetcenko, J. Alloys Compd. 480 (2009) 428–433.
[33] K. Young, T. Ouchi, W. Mays, B. Reichman, M.A. Fetcenko, J. Alloys Compd. 480 (2009) 434–439.
[34] K. Young, T. Ouchi, M.A. Fetcenko, J. Alloys Compd. 480 (2009) 440–448.